A Low-Cost, Fast, and Accurate Microwave Imaging System for Breast Cancer Detection

Daniele Jahier Pagliari[1], Azzurra Pulimeno[2], Marco Vacca[2], Jorge A. Tobon[2], Francesca Vipiana[2], and Mario R. Casu[2]
Politecnico di Torino, [1]DAUIN, [2]DET, Torino, Italy
Email: mario.casu@polito.it

Raffaele Solimene
Seconda Università di Napoli, Dip. Ing. Industriale e dell'Informazione, Napoli, Italy
Email: raffaele.solimene@unina2.it

Luca P. Carloni
Columbia University, Dept. Computer Science, New York, USA
Email: luca@cs.columbia.edu

***Abstract*—In this paper we present a prototype of a Microwave Imaging (MI) system for breast cancer detection. Our system is based on low-cost off-the-shelf microwave components, custom-made antennas, and a small form-factor processing system with an embedded Field-Programmable Gate Array (FPGA) for accelerating the execution of the imaging algorithm. We show that our system can compete with a vector network analyzer in terms of accuracy, and it is more than 20x faster than a high-performance server at image reconstruction.**

I. Introduction

Microwave Imaging (MI) for breast cancer detection exploits the dielectric contrast between malignant and healthy tissues [1]. Compared to mammography, MI can be safely repeated more frequently because it is free from ionizing radiations. It also removes the need for painful breast compression. Finally, it can also be a low-cost technique, which would make it competitive with high-resolution but very high-cost alternatives like MRI.

Two main approaches for MI have been proposed so far, *Ultra Wide-Band (UWB) Radar* and *Tomography*.

The radar approach consists in acquiring and processing UWB pulses reflected by the patient's breast tissues [2]. To work with UWB in the time-domain, ad-hoc new integrated circuits (ICs) are required [3][4][5]. It is also possible to work in the frequency-domain and reconstruct the pulses via FFT [6]. In this second case, besides developing new ICs [7], it is also possible to use sophisticated laboratory microwave instruments [8], which have the necessary flexibility to handle a large bandwidth with the required precision and accuracy. In any case, none of the implementations of the UWB radar approach that have been proposed so far can be classified as low-cost.

In the tomography approach a large bandwidth is not typically required and operations are done in the frequency-domain [1]. Even tough it is possible to build a low-cost tomography system, its main limitations stem from the need to solve an ill-posed, non-linear inversion problem [9]. Apart from convergence and stability, the main issue is execution time, because the non-linear inversion may take days of CPU.

We present a new approach to MI that has two distinctive properties. First, while working in the frequency domain, we use a relatively small bandwidth, i.e. 200 MHz between 1.4 and 1.6 GHz. Since low-cost off-the-shelf components are available in this frequency range, there is no need for ad-hoc designed ICs. Second, instead of non-linear inversion, we use a linear scattering inversion method called I-MUSIC [10], which aims at detecting the point of the breast that scatters the most the incident field. I-MUSIC requires the measured scattered electromagnetic field only at a few frequencies (e.g. 10) in the bandwidth of interest. Our method is fast because the processing phase can be run on an embedded processor, assisted by a field-programmable gate array (FPGA) for accelerating the most computationally intensive kernels. In addition, I-MUSIC does not require the knowledge of the response of the antennas, which reduces the cost of testing and calibration.

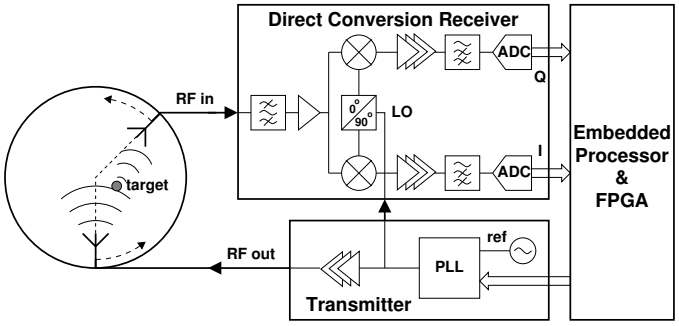

Fig. 1. Architecture of our breast-cancer detection Microwave Imaging system.

With our prototype, which we describe in Sec. II, we obtain results comparable in terms of accuracy to what a sophisticated microwave equipment can achieve, but at a small fraction of the cost. Moreover, our FPGA-enhanced embedded platform, described in Sec. III, accelerates the image reconstruction algorithm by more than 20x compared to a powerful multicore CPU. We obtain our experimental results with 2D phantoms, as discussed in Sec. IV. Our conclusions are in Sec. V.

II. System Architecture and Implementation

Fig. 1 depicts the architecture of our MI system, which is configured and supervised by the *embedded processor*. The *transmitter (TX)* is based on a PLL that synthesizes a frequency, configured by the processor, in the bandwidth of interest starting from a stable reference. A variable-gain amplifier controls the power of the *RF out* signal, which is sent to the transmitting antenna. The reflections created in the scene by a scatterer, e.g. a tumor target, are captured by a receiving antenna, which feeds the *receiver (RX)* with the *RF in* signal. The two antennas

978-1-4799-7234-0/15/$31.00 ©2015 IEEE

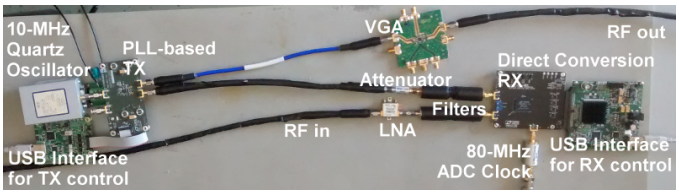

Fig. 2. Low-cost, small-size off-the-shelf components used in our MI prototype.

are placed around a circle at a fixed angle (135° in figure, but it can be any multiple of 45°), and a motor rotates them around the circle in such a way to scan the entire scene. Two antennas rotating at almost arbitrary angles give us more flexibility than antennas in fixed positions, and can *virtualize* a very large number of antennas. Moreover, by avoiding the complex switch matrix needed to multiplex TX and RX among multiple antennas [3][8], we eliminate a further source of cost and inaccuracy. The RX uses a *direct conversion (DC)* scheme in which the transmitted signal is also used as *local oscillator (LO)* to down-convert the received signal to base-band. Finally, *in-phase (I)* and *quadrature (Q)* signals are digitized and processed by the embedded processor, which is helped by the *FPGA*.

All parts of our prototype are off-the-shelf components, with the exception of the low-cost custom printed antennas. As shown in Fig. 2, the TX uses a Linear Technology LTC6946 chip, an ultra-low noise and spurious PLL Integer-N synthesizer with integrated VCO (0.5-dBm output power at 1.5 GHz), followed by a voltage-controlled variable-gain amplifier (VGA, gain range from -34 to +22 dB) by Analog Devices. The TX frequency is set via a USB-interface board. A 10-MHz oven-controlled crystal oscillator provides the reference frequency.

The input to the DC receiver undergoes band-pass filtering (Mini-Circuits component) and low-noise amplification (LNA, gain between 15 and 10 dB in the bandwidth, 1-dB max noise figure, also by Mini-Circuits). The RX is a Linear Technology LTM9004 chip, a 14-bit DC receiver with SNR 80 dB/MHz, typical noise floor -148.3 dBm/Hz, dynamic range 86 dB, minimum detectable signal -90 dBm (-105 dBm with the LNA). The LO signal is attenuated (6 dB) to avoid saturation. The digital values of the acquired signals, sampled with a 80-MHz clock, are sent via a USB-interface board to the processor (not shown in Fig. 2), the dual-core A9 ARM processor embedded in the Xilinx Zynq System-on-Chip. On the same die with the A9 processor, the Zynq features also the FPGA that we use to implement the specialized hardware that accelerates part of the imaging algorithm, as discussed in Sec. III. One of the well-known issues with DC receivers is the offset created by RF leakage, which is sensed and corrected by the processor in the calibration preceding the measurement phase.

Our low-cost custom antenna in Fig. 3(a) is printed on standard FR4 dielectric and connected to the other RF parts via an SMA connector. We designed and characterized the antenna using the finite-element method proposed in [11]. In particular, we obtained a good 50 Ω matching when the antenna is immersed in the coupling liquid, a lossy mixture of glycerin (80%) and water (20%) that reduces the scattering at the background/skin interface. Moreover, we could optimize the front profile to maximize the radiated near field. The S_{11} scattering parameter in Fig. 3(b) shows a good matching in a wide bandwidth, which includes the 1.4-1.6 GHz range.

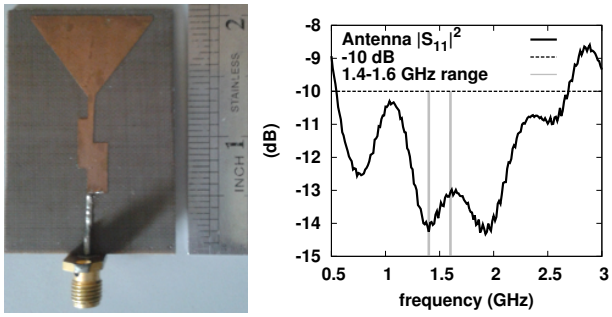

(a) (b)

Fig. 3. (a) Antenna and (b) S_{11} measured in 80-20% glycerin-water mixture.

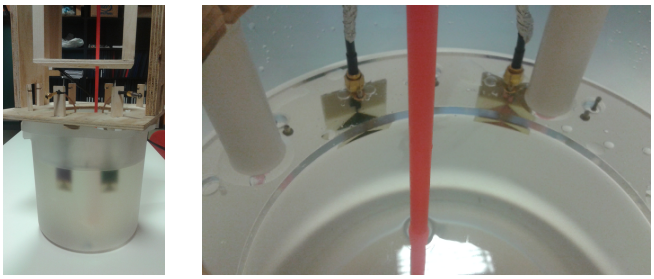

(a) (b)

Fig. 4. (a) Tank filled with glycerin-water mixture and the antennas. (b) Detail showing a vertically aligned cylinder representing the target of detection.

To perform our experiments, we immersed the antennas in a tank filled with the glycerin-water mixture, as shown in Fig. 4(a). In the example in figure, the angle between the antennas is 45°. A brushless motor mounted on top of the tank and controlled by the embedded processor rotates the two antennas. A wooden support permits the insertion of cylinders of different diameter and material which are kept vertically aligned, as shown in Fig. 4(b). These cylinders together with the coupling liquid form a 2D phantom. The cylinder is the target to be detected in our experiments.

III. Processing and Hardware Acceleration

The two rotating antennas acquire data at N frequencies in A angle positions, which the embedded processor elaborates to produce an image with possible malignant lesions highlighted. The imaging is obtained with the MUltiple SIgnal Classification-inspired (I-MUSIC) algorithm [10], which consists of two phases: clutter removal and reflected-energy map generation.

The clutter is due to a large scattering at the interface between the skin and the coupling medium. To remove it, I-MUSIC uses a subspace-projection method based on singular value decomposition (SVD). The matrix of the acquired data organized in N rows and A columns is transformed via SVD and the projections relative to the two dominant singular values are discarded to remove the clutter.

After clutter removal, an image is obtained through the steps in Listing 1. First, the eigenvalues of the correlation matrix $\mathbf{R} = S_d^n \cdot (S_d^n)^H$ are computed, where S_d^n is the nth row of the $N \times A$ decluttered samples matrix S_d. Through Hermitian inner product, the dominant eigenvector of $\mathbf{R}$ is multiplied with an array of Green functions, which model the propagation between the antennas and a point in the scanned surface that corresponds

Listing 1. MUSIC-Inspired computational kernel.

```
inv_P = 1;
for f = 1 : N % loop over frequencies
  R = Sd(:,:,f).' * conj(Sd(:,:,f)); % correlation matrix
  [V,D]=eig(R); % eigenvectors/eigenvalues computation
  [max_val, max_idx] = max(abs(diag(D)));
  for u = 1 : nx % loop over image rows
    for v = 1 : ny % loop over image columns
      % green function computation
      Wn = (exp(-j*kb(f) * sqrt((x(u)-xo).^2 +
           (y(v)-yo).^2)).').^2;
      % inner product and norm
      F(u,v,f)= norm((Wn / norm(Wn))' * V(:,max_idx));
    end
  end
  % product over different frequencies
  inv_P = inv_P.*(1-F(:,:,f).^2);
end
P = 1/inv_P;
```

to a pixel of the image. Therefore, to obtain the entire image, this step is repeated for all pixels and over all N frequencies (i.e. on all rows of S_d). At the end, a detection function P_f combines the results at different frequencies to obtain a peak in the image only for pixels that correspond to real scattering sources in the breast (i.e. tumors), while artifacts are rejected. More details on this procedure are available in [10].

In Listing 1, nx and ny represent the image size in pixels, $x(nx)$ and $y(ny)$ store the coordinates (with respect to the center of the scene) of the location under examination, xo and yo contain the positions of the antennas, and k_b is the wave number. Matrix P contains the detection function.

To be executed in a time span compatible with the duration of a medical examination, I-MUSIC needs hardware acceleration. In particular, since the execution time is dominated by the computation of Green functions and Hermitian Product, we designed an accelerator for that portion of the algorithm. The accelerator is implemented in the FPGA whereas the rest of I-MUSIC runs in software in the ARM processor. Instead of designing the accelerator directly in RTL using a hardware description language, such as Verilog or VHDL, we started from a higher level of abstraction. We described the accelerator in behavioral SystemC and used state-of-the-art commercial High-Level Synthesis (HLS) tools to synthesize the RTL description. The synthesized RTL is the entry point of the regular Xilinx FPGA design flow. By using this method, we could explore the design space more thoroughly than we could have done starting from RTL, in search of those micro-architectural solutions that obtain a lower execution time for the same use of FPGA resources. In particular, thanks to the capabilities of current HLS tools, we could explore the application of parallelism, pipelining, loop unrolling, and other design knobs, starting from a single high-level description. With this method, we validated around 100 design alternatives in about four months.

At the end of this process, we selected the design outlined in Fig. 5. Identical processing elements (PE) operate in parallel each on a *row* of the image. We chose the row as the atomic processing unit because it is a good balance between internal memory size of the accelerator and communication overhead. For each complex operation that a PE executes, such as division, square root, trigonometric function evaluation, etc, we used HLS to obtain a high-performance, pipelined implementation. Processor-Accelerator communication is also optimized. The accelerator has a system-bus slave interface for commands

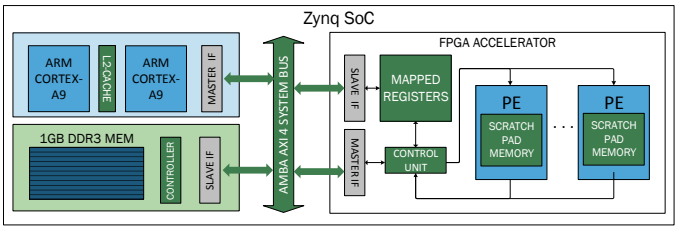

Fig. 5. I-MUSIC computing architecture on a Xilinx Zynq SoC.

and status information, and a master interface for DMA data transfers. Having performance as a goal, we synthesized the maximum number of PEs that fit on the Zynq. The FPGA executes the bottleneck part of I-MUSIC in less than 1 s independently on the input data, obtaining a speed-up greater than 20x with respect to a software execution on a server-class Intel multicore (Xeon E5-2643 @3.30 GHz, 64 GB RAM).

IV. Experimental Results

To evaluate the detection capabilities of our prototype, we experimented with tumor phantoms represented by small-diameter cylinders of different materials immersed in the tank. In particular, we report results obtained with a 12-mm diameter metallic cylinder, which mimics a highly reflective tumor, and with a 20-mm diameter plastic dielectric cylinder filled with a 40%-60% glycerin-water mixture, which creates a much slighter dielectric contrast with the coupling liquid ($\sim$4:1).

We obtained 18 measurements by rotating the antennas around the target in steps of 20°. We acquired the measured data both with our system and with a broadband Vector Network Analyzer (VNA) in order to make a comparison. With our system, we explored the bandwidth between 1.4 GHz and 1.6 GHz, which is where the receiver is best matched, in 20-MHz steps. With the VNA, we acquired the data in the same bandwidth for a fair comparison, but we could also scan the investigated scene in a larger bandwidth from 0.5 to 2.0 GHz. In this way, with the first set of measurements we could determine the accuracy of our system compared to the VNA, and with the second set we could evaluate if relevant information is lost when restricting the investigation to the 1.4-1.6 GHz range.

The images that we obtained after running I-MUSIC on the acquired data are reported in Fig. 6. The yellow circle identifies the actual target, while the colored shades highlight the scattering points detected by the algorithm.

Figs. 6(a)-(c) refer to the case of the metallic cylinder. In this case the angle between the antennas was 135°. Figs. 6(a)-(b) are obtained with the VNA in the full 0.5-2.0 GHz range and in the sub-range between 1.4 and 1.6 GHz, respectively: We do not observe a significant loss of information. Fig. 6(c) is obtained with our system, which is able to correctly detect the target, albeit slightly shifted.

Figs. 6(d)-(f) are obtained with the dielectric cylinder. The angle between the antennas was 45°. In this case, additional frequencies in the full range slightly improve the focus of the detected point, as we can see by comparing Fig. 6(d), obtained with the VNA in the full 0.5-2.0 GHz range, with Fig. 6(e), obtained in the 1.4-1.6 GHz range. Fig. 6(f) shows that not only our system correctly detects the target, but the focus is better than what the VNA obtains in the same frequency range.

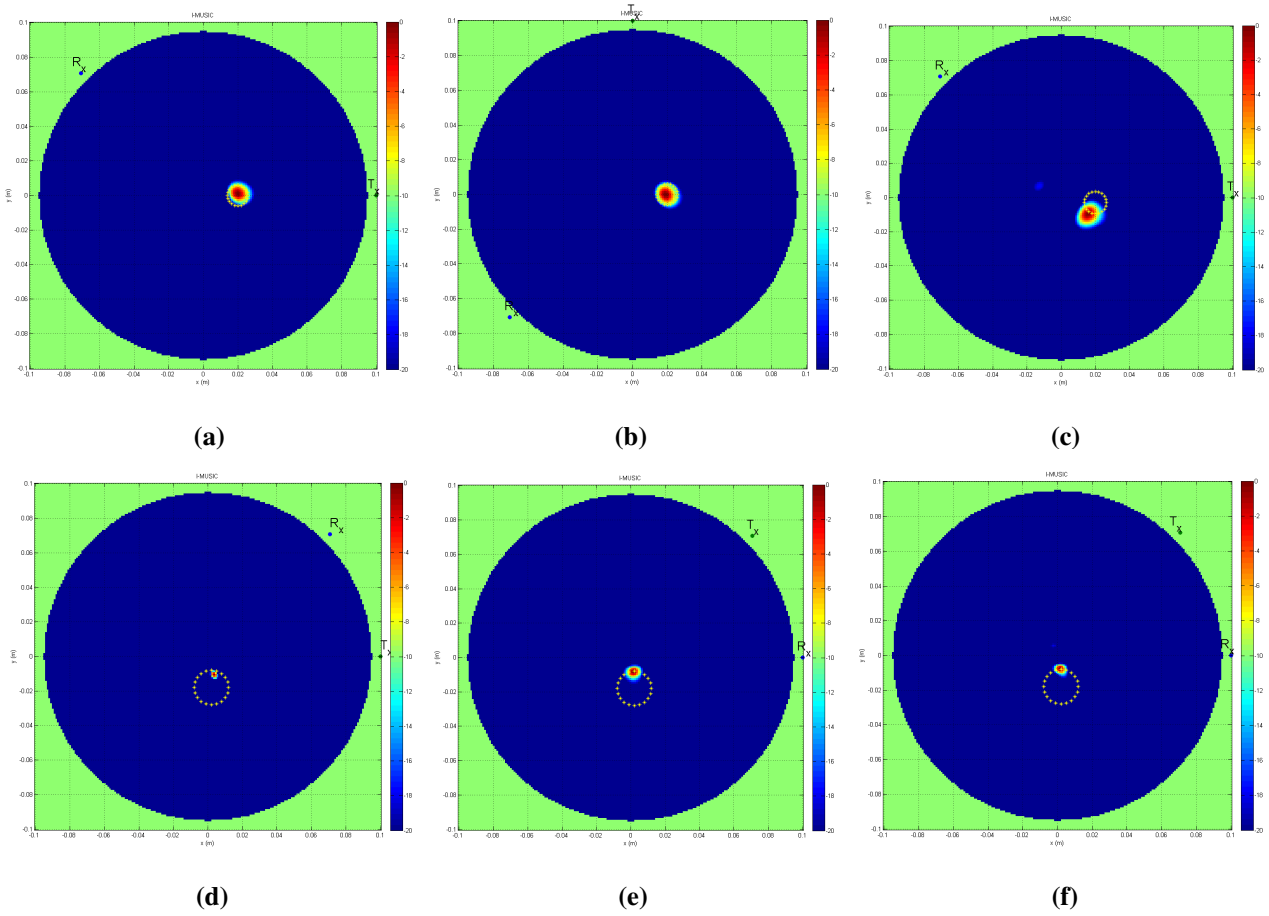

Fig. 6. Maps obtained with I-MUSIC, (a)-(c) 12-mm metallic target, (d)-(f) 20-mm cylinder filled with 40%-60% glycerin-water mixture. (a) and (d) obtained with the VNA, 0.5-2.0 GHz ; (b) and (e) obtained with the VNA, 1.4-1.6 GHz; (c) and (f) obtained with our system.

V. Conclusions

We presented a low-cost, fast, and accurate system for breast cancer detection using microwave imaging. The system is low-cost because it uses off-the-shelf components and in-house fabricated antennas. It is fast because it executes the imaging algorithm more than 20x faster than a multicore CPU thanks to the use of FPGA hardware acceleration. Finally, our experimental results show that detection is possible with accuracy similar to what can be achieved using standard costly microwave equipment such as a vector network analyzer.

Acknowledgment

This work is supported by the Italian Ministry of University and Research under FIRB project MICENEA and in part by the National Science Foundation (A#: 1219001).

References

[1] P. M. Meaney, M. W. Fanning, D. Li, S. P. Poplack, and K. D. Paulsen, "A clinical prototype for active microwave imaging of the breast," *IEEE Trans. Microw. Theory Tech.*, vol. 48, no. 11, pp. 1841–1853, 2000.

[2] S. C. Hagness, A. Taflove, and J. E. Bridges, "Two-dimensional FDTD analysis of a pulsed microwave confocal system for breast cancer detection: Fixed-focus and antenna-array sensors," *IEEE Trans. Bio-Med. Eng.*, vol. 45, no. 12, pp. 1470–1479, 1998.

[3] A. Azhari, S. Takumi, S. Kenta, T. Kikkawa, and X. Xiao, "A 17 GHz bandwidth 1.2 mW CMOS switching matrix for UWB breast cancer imaging," in *Proc. IEEE BioCAS*, 2014, pp. 109–112.

[4] Y. Seo *et al.*, "CMOS equivalent time sampling of gaussian monocycle pulse for confocal imaging," in *Proc. IEEE BioCAS*, 2014, pp. 125–128.

[5] X. Guo, M. R. Casu, M. Graziano, and M. Zamboni, "Simulation and design of an UWB imaging system for breast cancer detection," *Integration, the VLSI Journal*, vol. 47, no. 4, pp. 548–559, 2014.

[6] E. J. Bond, X. Li, S. C. Hagness, and B. D. Van Veen, "Microwave imaging via space-time beamforming for early detection of breast cancer," *IEEE Trans. Antennas Propag.*, vol. 51, no. 8, pp. 1690–1705, 2003.

[7] M. Bassi, A. Bevilacqua, A. Gerosa, and A. Neviani, "Integrated SFCW transceivers for UWB breast cancer imaging: Architectures and circuit constraints," *IEEE Trans. Circuits Syst. I*, vol. 59, no. 6, pp. 1228–1241, 2012.

[8] M. Klemm *et al.*, "Microwave radar-based differential breast cancer imaging: imaging in homogeneous breast phantoms and low contrast scenarios," *IEEE Trans. Antennas Propag.*, vol. 58, no. 7, pp. 2337–2344, 2010.

[9] T. M. Grzegorczyk, P. M. Meaney, P. A. Kaufman, R. M. di Florio-Alexander, and K. D. Paulsen, "Fast 3-D tomographic microwave imaging for breast cancer detection," *IEEE Trans. Med. Imag.*, vol. 31, no. 8, pp. 1584–1592, 2012.

[10] G. Ruvio, R. Solimene, A. Cuccaro, and M. J. Ammann, "Comparison of noncoherent linear breast cancer detection algorithms applied to a 2-D numerical model," *IEEE Antennas Wireless Propag. Lett.*, vol. 12, pp. 853–856, 2013.

[11] E. Attardo, A. Borsic, G. Vecchi, and P. M. Meaney, "Whole-system electromagnetic modeling for microwave tomography," *IEEE Antennas Wireless Propag. Lett.*, vol. 11, pp. 1618–1621, 2012.